Spectroscopic properties of explosive volcanism within the Caloris basin with MESSENGER observations

S. Besse, A. Doressoundiram, J. Benkhoff

AGU PUBLICATIONS

JGR

Journal of Geophysical Research: Planets

RESEARCH ARTICLE
10.1002/2015JE004819

Key Points:
- The VIS and NIR spectra are reconciled to use spectra from 300 nm to 1450 nm
- Pyroclastic deposits have different spectral properties from Mercury average
- Spectral properties are consistent with a low iron content or a change in grain size

Correspondence to:
S. Besse,
sbesse@sciops.esa.int

Citation:
Besse, S., A. Doressoundiram, and J. Benkhoff (2015), Spectroscopic properties of explosive volcanism within the Caloris basin with MESSENGER observations, *J. Geophys. Res. Planets*, *120*, 2102–2117, doi:10.1002/2015JE004819.

Received 12 MAR 2015
Accepted 4 NOV 2015
Accepted article online 9 NOV 2015
Published online 2 DEC 2015

Spectroscopic properties of explosive volcanism within the Caloris basin with MESSENGER observations

S. Besse[1], A. Doressoundiram[2], and J. Benkhoff[1]

[1]ESA/ESTEC, Noordwijk, Netherlands, [2]LESIA, Observatoire de Paris, Meudon, France

Abstract Volcanism on Mercury has been indisputably identified at various locations on the surface, by means of both effusive and explosive volcanism. Its characterization is crucial to understand the evolution of the planet, in particular the thermal evolution of the mantle, and the volatile content of the planet. This analysis presents a detailed view of the pyroclastic deposits of the Caloris basin. Observations from the Mercury Atmospheric and Surface Composition Spectrometer (MASCS) are used to understand the spectral characteristics of the pyroclastic deposits, both in the visible and near-infrared. Additional calibration steps are proposed to reconcile the difference of absolute reflectance between the visible (VIS) and near-infrared (NIR) detectors. These calibration steps allow the use of the full spectral range of the MASCS instrument. Pyroclastic deposits exhibit a redder spectral slope in the VIS and NIR. This spectral slope diminishes toward the edge of the deposits to match that of Mercury's average surface. Spectral properties in the ultraviolet (UV) also change as a function of distance to the vent. Only the UV properties unambiguously separate the pyroclastic deposits from Mercury's average spectra. The spectral variations are consistent with a lower iron content of the pyroclastic deposits with respect to the average surface of Mercury, similar to what has been proposed for pyrolcastic deposits on the lunar surface. Nonetheless, given the limited illumination conditions diversity of the MASCS instrument, other causes such as grain size, space weathering, and bulk composition could also be accounted for the spectral variations. Variability of the pyroclastic deposits' properties within the entire basin are potentially identified between the three main clusters, and could be related to space weathering of deposits of different ages.

1. Mercury's Volcanism

Since the first observations of the surface of Mercury through the Mariner 10 images, volcanism had been suspected to explain the origin of the large smooth regions of the northern hemisphere [*Strom et al.*, 1975; *Murray et al.*, 1975]. But only with the next generation of space observations from the MErcury Surface, Space ENvironment, GEochemistry, and Ranging (MESSENGER) spacecraft [*Solomon et al.*, 2007, 2011] has the volcanic origin of the smooth plains become evident [*Head et al.*, 2011, 2008; *Prockter et al.*, 2010; *Denevi et al.*, 2013]. In fact, the volcanic smooth plains represent 18% of Mercury's surface [*Denevi et al.*, 2013], highlighting that volcanism on Mercury is an important process that has shaped the surface of the planet. The smooth plains exhibit a wide range of spectral variations that usually distinguish them from the average terrain [*Denevi et al.*, 2009]. Measurements from the MESSENGER X-ray Spectrometer confirm the mafic to ultramafic composition of these low-iron basalt-like smooth plains [*Nittler et al.*, 2011; *Weider et al.*, 2012], which may have been emplaced by subsequent voluminous low-viscosity and high-effusion lavas [*Head et al.*, 2011; *Byrne et al.*, 2013], similar to those forming the lunar maria but with much lower iron content.

Additionally, evidence of volcanism by means of explosive eruptions, in contrast to effusive volcanism associated with the smooth plains, has also been spotted in various places on Mercury's surface [*Kerber et al.*, 2011]. Spectrally, the deposits are brighter and redder than the average terrain of Mercury [*Kerber et al.*, 2011]. Up to 200 pyroclastic deposits have been proposed based on their spectral properties [*Kerber et al.*, 2014], along with additional candidates based on morphological characteristics of irregular pits [*Thomas et al.*, 2014a]. The pyroclastic deposits are typically not seen within the smooth plains, possibly because they have been covered by subsequent lava flows. For instance, the deposits appear mostly along the rim of the Caloris basin.

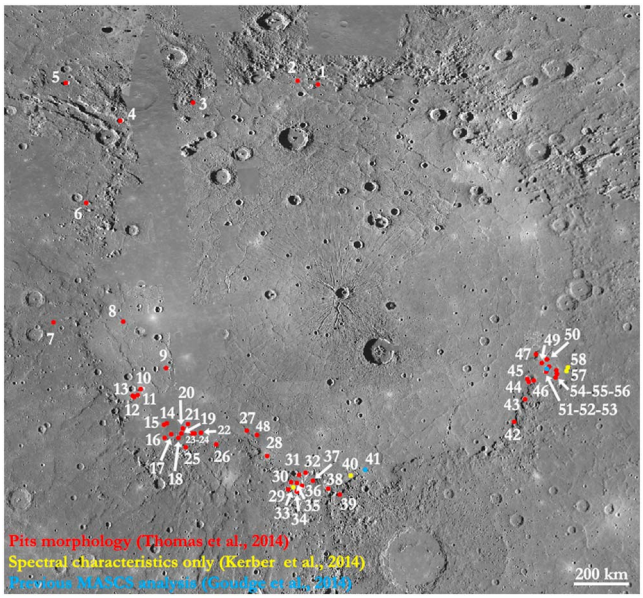

Figure 1. Distribution of the pyroclastic deposits in and around the Caloris basin. Most of the deposits and vents are located in the southern portion of the basin. The figure compiles the candidates from *Kerber et al.* [2011] and *Thomas et al.* [2014a]. The red dots correspond to candidates identified by *Thomas et al.* [2014a], the yellow dots candidates identified by *Kerber et al.* [2011, 2014] only, and the blue dot is the candidate analyzed by *Goudge et al.* [2014] that has not been identified by *Thomas et al.* [2014a]. Candidates 13, 21, and 38, although marked in red, have been also analyzed by *Goudge et al.* [2014].

There are of course notable exceptions [*Rothery et al.*, 2014], which could be interpreted to suggest that explosive volcanism probably lasted longer than effusive volcanism. In fact, *Thomas et al.* [2014b] have shown that explosive volcanism occurred from at least 3.9 Ga until less than a billion years ago. This result suggests that explosive volcanism was substantially longer-lived than effusive volcanism (i.e., smooth plains) that has been dated from ~ 4.1 to 3.55 Ga [*Marchi et al.*, 2013].

The interior of the Caloris basin is filled by smooth plains of volcanic origin and represents a large fraction of the smooth plains on the whole planet [*Denevi et al.*, 2013] (Figure 1). Both explosive and effusive volcanism have been recognized in the basin [*Murchie et al.*, 2008; *Head et al.*, 2008]. Explosive volcanism is mostly located at the edges of the basin [*Kerber et al.*, 2011, 2014; *Thomas et al.*, 2014a], and effusive volcanism fills the interior to a thickness of up to 3.5 km [*Ernst et al.*, 2015].

This peculiar distribution of the pyroclastic deposits may reflect their relatively young age [*Thomas et al.*, 2014b] with respect to the effusive volcanism that fills the entire basin [*Ernst et al.*, 2015]. In fact, the subsurface structure of the Caloris basin should have many faults that penetrate deeper into the interior of Mercury at the edge of the basin [*Klimczak et al.*, 2013], thus favoring a deeper source for explosive volcanism, as often suggested for the Moon [*Gaddis et al.*, 2003]. *Klimczak et al.* [2010] also suggests that the center part of Caloris, Pantheon Fossae, is most likely to have been formed as the result of doming in the central part, probably caused by a magma chamber. If confirmed, this doming would have made access to the surface more difficult for late-stage volcanism, and this could explain why no candidates for explosive volcanism are identified in the central part of Caloris.

One of the first noticeable facts from Figure 1 is that the majority of the candidate pyroclastic deposits, and the three clusters of candidates (i.e., candidates 9–26, candidates 29–41, and candidates 42–58), are distributed along the southern edge of the basin. *Goudge et al.* [2014] analyzed four pyroclastic deposits from the first two clusters, finding different characteristics for the UV properties with respect to Mercury's average spectrum. Additionally, the authors found that based on crater degradation, a significant portion of the pyroclastic deposits span between 4.0 and 1 Ga. However, based on the very low statistics (i.e., only four deposits studied in Caloris), the authors did not conclude on any variability of the pyroclastic deposits (i.e., composition, spectral slope, age, and grain size) within the Caloris basin.

In this analysis, with the use of the MESSENGER observations by the visible to near-infrared spectrometer, the objective is to better characterize the pyroclastic deposits of the Caloris basin, to evaluate their common characteristics, and to determine whether the three clusters of deposits are contemporary with one another, or represent a sequence of events that may result in variable spectral properties. These analyses use a larger number of pyroclastic deposits and use the spectral observations from 300 to 1400 nm, while *Goudge et al.* [2014] stopped at 800 nm due to the difficult calibration of the observations in the longer wavelength domain.

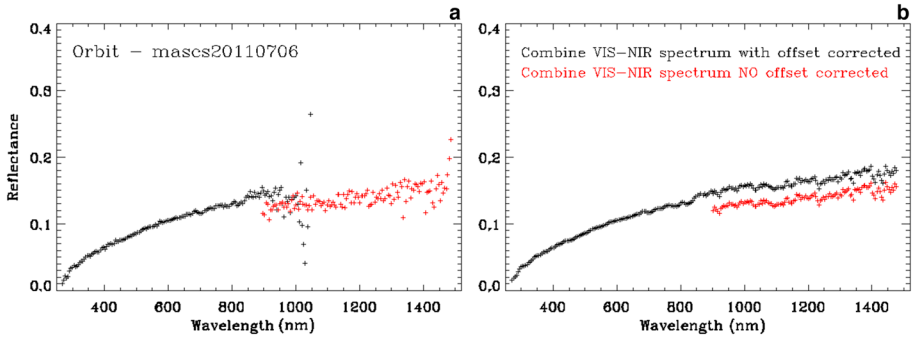

Figure 2. Typical spectral output from the MASCS observations in the PDS archive. (a) The calibrated spectra show a better signal in the VIS (black) with respect to the NIR (red). In the overlap range of the two detectors (900–1050 nm), the VIS detector shows a rapid decrease in the signal. (b) The same spectra after additional corrections, with (black) or without (red) the offset correction.

2. MESSENGER Observations

2.1. Mercury Atmospheric and Surface Composition Spectrometer

The Mercury Atmospheric and Surface Composition Spectrometer (MASCS) is part of a science instrument suite onboard the MESSENGER spacecraft [*McClintock and Lankton*, 2007]. The telescope simultaneously feeds the ultraviolet and visible spectrometer (UVVS) and the Visible and Infrared Spectrograph (VIRS); only the VIRS is considered in this study. VIRS is a point spectrometer covering the wavelength range 300–1450 nm at 5 nm resolution using two separate detectors. The (visible) VIS detector is usually used from 300 to 900 nm, while the near-infrared (NIR) detector extends from 900 to 1450 nm. In fact, the VIS detector extends to 1050 nm, providing detector overlap between 900 and 1050 nm, which could be potentially used to adjust the absolute reflectance of the VIS and NIR detectors. In this study, we use the calibrated MASCS data available from the Planetary Data System (PDS). The data are radiometrically [*Holsclaw et al.*, 2010], and photometrically [*Izenberg et al.*, 2014] calibrated, although the photometric correction is done to a viewing geometry of $i = 45°$, $e = 45°$, $\alpha = 90°$, different from the typical corrections done on other planets ($i = 30°$, $e = 0°$, $\alpha = 30°$) [e.g., *Besse et al.*, 2013].

It is important to state at this point that the MASCS observations are taken with extremely large phase angles, no observations below 78° are available. This somehow unusual conditions for spectroscopy complicates the interpretation of the data. Additional causes with respect to mineralogical variations could also play an important role in the spectral variability, in particular the grain size which is an important product of pyroclastic deposits.

2.2. VIS-NIR Instrument Corrections

As noted by *Izenberg et al.* [2014], the instrument temperature can vary from 10°C to >50°C. The NIR detector is more sensitive to background signal and elevated temperature, resulting in a typical signal-to-noise ratio (SNR) 3–5 times lower than the VIS detector. The VIS range from 800 to 1050 nm also suffers from a decrease of the SNR with respect to the visible part (300–800 nm) (Figure 2). This is due to the drastic drop in the sensitivity of the detector after 900 nm. In fact, *Goudge et al.* [2014] decided to limit the spectral analysis of the pyroclastic deposits to 800 nm in order to avoid the lower SNR at the end of the VIS detector wavelength range. Additionally, there is a reflectance discrepancy between the VIS and the NIR, as can be seen in Figure 2. At the time of writing, and despite many efforts from the MESSENGER team, no correlation has been found between the reflectance offset and a specific parameter (e.g., temperature and phase angle). Unfortunately, this limits the analysis of the NIR portion of the MASCS observations, unless specific corrections are performed to match the reflectance of the two detectors.

In this study, a specific algorithm is designed to automatically adjust the reflectance of the NIR and VIS detectors. This type of correction has been also done by *Izenberg et al.* [2014], although they have not provided all the details. For this analysis, it is assumed that

1. The absolute reflectance of the VIS is correct and the NIR should be adjusted to the VIS. *Holsclaw et al.* [2010] reported that the absolute reflectance of the VIS detector is correct, with a 10% error. The VIS detector is also significantly less sensitive to temperature variations. Therefore, given that the NIR detector has generally

lower reflectance than the VIS (up to 50% lower, much larger than the 10% error of the VIS), the assumption of matching the reflectance of the NIR detector to the VIS is valid.
2. The spectral slopes of both detectors are correct, and only an offset correction is needed for the NIR.

Assuming the above, the correction is performed to match the reflectance of the NIR detector to the VIS. Additionally, the correction also limits the scattering of the channels with a smoothing, in particular, for the NIR. The correction is performed in three steps as described:

1. Removal of the outliers. For the VIS, the channels that are above the 2 sigma deviation from the mean in the range 800–950 nm, where the VIS SNR is poor, are removed. The channels above 950 nm are systematically removed because of their large excursions. For the NIR, the channels that are above the 2 sigma deviation from the mean in the range 900–1450 nm are removed. It is noted that for both detectors, the spectral slope is not accounted for in deriving the 2 sigma deviation. However, at this stage, only removing the large outliers is important.
2. Smoothing of the spectral signal. A moving average window of three points is applied to the entire NIR and VIS domains to remove the scatter of the channel-to-channel reflectance. The effect is mostly seen in the NIR detector where the SNR is lower.
3. Applying an offset correction to the NIR. Offset correction is extremely challenging because to adjust the absolute reflectance of the NIR, the right offset must be determined in order to conserve the slope of the spectra and to preserve any slight absorption bands that could be present in the 800–1200 nm region. Unfortunately, the overlap region between the two detectors also shows a rapid decrease of the SNR in the VIS with very large excursions from the mean. For this reason, the overlap region could not be used to straightforwardly derive the offset, and removing the outliers often resulted in keeping too few channels in the VIS overlap region. To match the two detectors' reflectance, *Izenberg et al.* [2014] used a combination of binning and averaging of the last 40 nm of the VIS and the first 40 nm of the NIR. This approach is, however, very sensitive to noise, which is an issue in both the VIS and NIR. In order to be less sensitive to the noise, a larger region should be used to compare the VIS and NIR detectors. Unfortunately, the overlap region corresponds exactly to the lower SNR region of the VIS detector. In this work, we rely on the portion of the VIS spectra with high SNR (shorter than 800 nm), and extrapolate it to the overlap region to be compared with the NIR. The domain 600–750 nm, which does not contain mafic absorption bands, is fitted by a straight line that is extrapolated to 1050 nm. Then, the average of the signal extrapolated in the VIS between 900 and 1050 nm is compared to the NIR average of the same wavelength domain. The advantage of this approach is the robustness to the noise. The main disadvantage is in the extrapolation, which could remove any hints of absorption bands around 1000 nm.

Ultimately, the original smoothed and outlier-free spectra from the VIS detector between 300 and 900 nm is merged with the smoothed and offset spectra of the NIR detector, which also has outliers removed. An example final spectrum is given in Figure 2, with and without the offset correction applied.

2.3. Application to Lunar Spectra

In order to better qualify and quantify the different approaches to match the reflectance of the NIR and VIS detectors, the methods have been applied to lunar spectra of pyroclastic deposits and a typical lunar soil with very small absorption bands at 1000 nm. Given the very low iron content of Mercury's surface, mature lunar highland spectra have similar spectral slope and absorption bands to Mercury's surface. They are good analogs to test the correction described in section 2.2. Lunar spectra were extracted from the Moon Mineralogy Mapper observations and resampled to the MASCS VIS and NIR spectral resolution. In order to test the offset correction, the NIR lunar spectra are systematically offset with a value of −0.01, which is within an order of magnitude of the MASCS-NIR offsets.

Two of several tests are presented in Figure 3. Figure 3a corresponds to lunar feldspathic material from the farside, with a small absorption band close to 1000 nm (∼1%). The black line is the original spectrum, the blue line corresponds to the approach described in section 2.2, the orange line to the approach of *Izenberg et al.* [2014]. The method of extrapolating the visible to calculate the offset is efficient in this case and retrieves the offset with reasonable accuracy (i.e., 0.0105). The method of averaging the end of the VIS and the beginning of the NIR is less successful (i.e., 0.0072). This is explained by the fact that the comparison is not done on the same wavelengths domain, and the correction is therefore sensitive to the slope and the noise. In fact, unless the slope is null (which is not the case on the surface of Mercury or the Moon), this approach will always

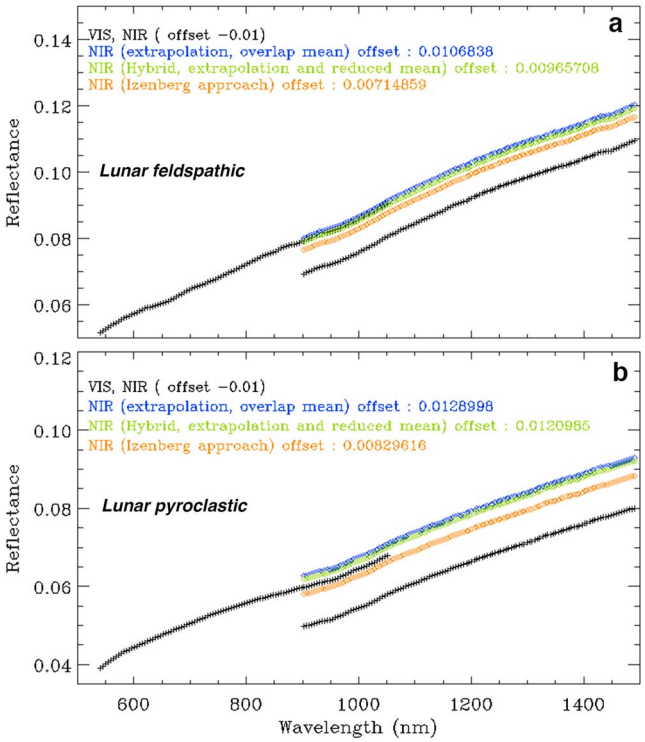

Figure 3. Examples of the algorithm outputs on lunar spectra. (a) Typical lunar mature feldspathic material from the far side. (b) Lunar pyroclastic deposits from the Alphonsus crater [*Jawin et al.*, 2015]. The correction works better if the absorption bands are minimal.

underestimate the offset, as can be seen in both examples. Because the VIS-extrapolation approach uses the same region to calculate the offset, it is less affected by the slope. However, if there were a strong difference in the VIS slope (i.e., 600–750 nm) and the NIR slope (i.e., 900–1050 nm), the offset correction will be less accurate. Additionally, given the highly reducing environment of Mercury, such a break in slope along the wavelength domain is highly unlikely. Experience with Mercury's spectra shows that the difference is small enough, thus this approach should provide an accurate correction. An alternative hybrid correction is tested in green, where the average of a smaller portion of the extrapolated VIS is used (i.e., 900–960 nm), and the NIR is kept to the overlap region (i.e., 900–1050 nm). In this case, the offset is slightly underestimated, and the cause is the same as that in Izenberg's approach.

Figure 3b corresponds to pyroclastic deposits from the Alphonsus crater on the lunar near-side. A prominent absorption band around 1000 nm is visible both in the VIS and NIR spectra (~4–5%). In this case, none of the approaches retrieve a good offset, in particular, because the extrapolation of the VIS does not take into account the absorption band. Therefore, the VIS extrapolation is systematically overestimating the offset, while the Izenberg's approach is still underestimating it.

Thus, utmost care should be taken to ensure that the correct offset is calculated, and potential absorption bands are not erased. To overcome that issue, qualitative parameters are calculated to evaluate the quality of the correction:

1. VIS-NIR slope, which compares the slope in the VIS (i.e., 600–750 nm) and in the NIR (i.e., 900–1050 nm). This parameter helps to evaluate whether the offset correction should be changed because of important variations in the slope.
2. Extrapolation-Real VIS, which compares the averaged reflectance of the original and extrapolated VIS in the 750–800 nm. This parameter helps to evaluate if the slope is changing in a region where mafic absorptions are expected to start.

By using the correction described in section 2.2, and with quality checked of the above parameters, the VIS and NIR spectra can be combined (Figure 2) and analyzed with reasonable confidence.

2.4. Caloris Survey

The Caloris basin has been observed many times during the orbital phase of the mission and also during the previous flybys. Its diameter is about 1500 km [*Fassett et al.*, 2009], with its interior covered by smooth plains that are common in the northern hemisphere [*Denevi et al.*, 2013]. The smooth plains have a volcanic origin, more precisely an effusive volcanism type [*Head et al.*, 2008] that is undercut by numerous irregular vents [*Thomas et al.*, 2014a], with color variations [*Kerber et al.*, 2011] that are attributed to explosive volcanism and pyroclastic deposits candidates. As can be seen in Figure 1, the deposits are preferentially located in the southern part of the basin. This bias is unlikely to be due to observing conditions, since the resolution decreases with southern latitude and thus the opposite distribution would be expected (i.e., more detection to the north

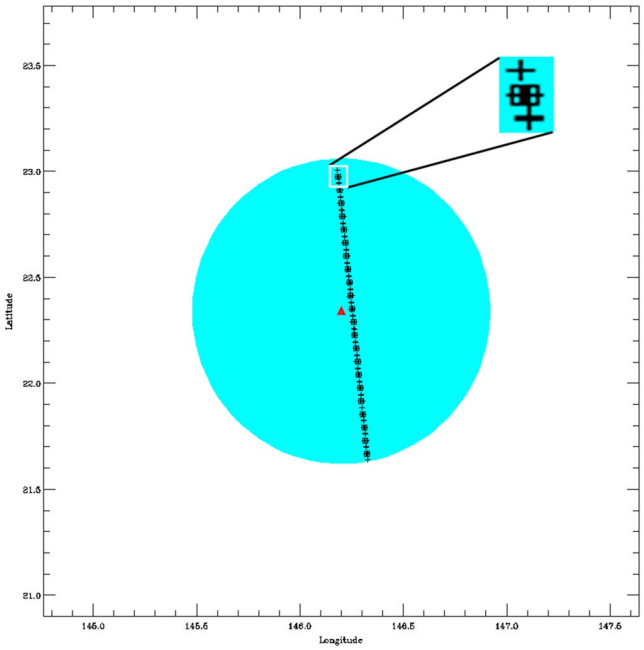

Figure 4. Example of the footprint selection of one orbit over the pyroclastic deposit number 10. The blue circle corresponds to the extent of the deposits and the red triangle to the center of the deposit. The insight is a zoom over one footprint, crosses correspond to the four corners of the footprint, while the empty square corresponds to the center of the footprint. In this case, the footprint is very elliptic; thus, two of the corners are located very close to the center. The extent of the deposits is not known with a very accurate precision; therefore, a margin could be applied in the selection of the footprints (see text for more details).

where the resolution is higher). *Thomas et al.* [2014b] performed a thorough investigation of the irregular pits of Mercury's surface, including Caloris. More than 50 pyroclastic deposits have been proposed in the Caloris basin, mostly based on the possible identification of vents, but also based on color anomalies. This detection is the basis of the catalog of pyroclastic deposits proposed on Figure 1. *Kerber et al.* [2014, 2011] identified many pyroclastic deposits candidates, mostly from a spectral point of view. They are represented in yellow in Figure 1, only if not reported by *Thomas et al.* [2014a]. Additionally, we marked in blue the spectral analysis done by *Goudge et al.* [2014] and not identified by *Thomas et al.* [2014a], since they are highly relevant for this analysis. Pyroclastic deposits candidates 13, 21, and 38 have also been spectrally studied [*Goudge et al.*, 2014] and identified by *Thomas et al.* [2014a]; thus, they appear red on the map.

In order to focus on the three clusters of deposits shown in Figure 1, candidates 1 to 8 are not analyzed. MASCS observations of deposits 9 to 58 were extracted from the PDS database for this analysis. These data include observations made during the flybys and during the orbital phase of the mission. The photometric correction [*Izenberg et al.*, 2014] minimizes the effect of varying illumination conditions, thus allowing the use of observations from multiple phases of the mission. It is important to note that since the analysis of *Goudge et al.* [2014], many more observations are available.

Given the variability in the range of illumination conditions and resolution of the MASCS instrument, only the orbits with footprints located within the extend of the deposits, and with spatial resolutions not exciding the extent of the deposits are selected. This is illustrated in Figure 4, where only the footprints located within the deposit are selected for the analysis. In a first step, footprints located outside the deposits are selected with a margin of 10 % of the radius of the deposits. This is done to accommodate for possible larger extent of the deposits then previously mapped. In a second step, spectral parameters are used to refine the extend of the deposit. As will be seen in section 3.1, the VIS slope as a function of distance to the vent can be used to track the limit of the deposits, assuming that if the value is above 1 (i.e., higher than Mercury's average), the footprints are still located within the deposits. This results in a final selection of the radius of the deposits that could be larger or smaller than the one previously mapped (e.g., Table 1, sixth and seventh columns).

A summary of the pyroclastic deposits and the observations is given in Table 1.

3. Results

3.1. Spectral Parameters

In order to characterize the spectral properties of the pyroclastic deposits, a number of parameters are defined. They encompass the entire spectral range of MASCS (i.e., 300 to 1450 nm), with emphasis on both the VIS and NIR. The parameters are summarized in Table 2.

Table 1. Summary of the Pyroclastic Deposits in and Around Caloris, Their Location, and the Spectral Observations Used

No.[a]	ID[b]	Name[c]	Lattitude[d]	Longitude[e]	Radius[f]	R. U.[g]	Nb_O[h]	Nb_S[i]	Nb_S U.[a]	Spatial E.[b]
1	4037	-	48.40	161.23	5.0	-	-	-	-	-
2	6007	-	48.69	159.48	9.5	-	-	-	-	-
3	6156	-	46.86	150.56	7.2	-	-	-	-	-
4	6099	-	45.32	144.35	5.1	-	-	-	-	-
5	6044	-	48.49	139.67	-	-	-	-	-	-
6	6014	-	38.28	141.47	14.3	-	-	-	-	-
7	6087	-	28.02	138.62	5.9	-	-	-	-	-
8	6102	-	28.10	144.64	7.3	-	-	-	-	-
9	6111	-	24.21	148.38	11.5	20	2	10	7	0.35
10	6062	RS-03 Main	22.34	146.20	24/28.3	30	5	85	43	0.50
11	6062	-	22.34	145.81	-	-	-	-	-	-
12	6062	RS-03 SW	21.57	145.54	19.3	20	1	3	3	0.18
13	6062	RS-03 SW	21.83	145.32	19.3	20	-	-	-	-
14	6160	-	19.45	148.34	7.4	8.0	1	5	3	0.16
15	6160	-	19.30	148.11	5.1	6	2	4	4	0.14
16	6160	-	18.21	148.16	14.7	15	2	8	6	0.30
17	6160	-	18.57	148.72	-	-	-	-	-	-
18	6071	-	18.19	149.30	4.7	5.0	1	1	1	0.13
19	6071	-	18.52	149.56	-	6.0	1	2	1	0.13
20	6071	-	18.95	149.70	-	-	-	-	-	-
21	6071	RS-03 SE	19.36	150.16	7/14.5	15.0	4	20	9	0.28
22	6155	-	18.66	151.28	4.2	-	-	-	-	-
23	6155	-	18.56	150.67	12.7	15.0	1	3	1	0.29
24	6155	-	18.51	150.73	12.7	-	-	-	-	-
25	6157	-	17.36	149.95	7.8	8.0	2	7	5	0.16
26	6153	-	17.65	152.57	5.9	6.0	1	1	1	0.14
27	6084	-	18.80	155.20	-	20.0	4	16	10	0.38
28	6067	RS-04b	16.65	156.91	19/31.0	32.0	3	26	13	0.6
29	6016	-	13.79	158.75	-	15.0	1	3	3	0.30
30	6016	-	14.37	158.95	-	-	-	-	-	-
31	6016	-	15.01	159.58	-	15.0	1	3	3	0.35
32	6016	-	15.20	160.17	-	-	-	-	-	-
33	6016	RS-04a	14.10	159.20	19/43.6	45.0	3	26	17	0.85
34	6016	-	13.59	159.43	-	15.0	-	-	-	-
35	6016	-	14.34	159.50	-	15.0	1	3	3	0.30
36	6016	-	14.09	159.94	-	-	-	-	-	-
37	6016	-	14.49	160.79	5.9	6.0	-	-	-	-
38	4015	RS-04c	13.84	162.08	19	20.0	3	13	9	0.35
39	4015	-	13.33	163.13	19	-	-	-	-	-
40	-	RS-04d	15.00	164.00	17	17.0	2	11	4	0.30
41	-	RS-04e	15.40	165.30	12	12.0	3	11	8	0.25
42	4044	-	19.50	178.07	3.5	20.0	3	13	7	0.36
43	4001	-	21.50	178.97	6.4	7.0	1	2	2	0.14
44	4038	-	22.95	179.28	12.6	20.0	2	7	5	0.43
45	4038	-	23.24	179.15	-	20.0	2	10	5	0.41
46	4038	-	23.09	179.67	-	-	-	-	-	-
47	4010	-	25.32	-179.87	31.7	-	-	-	-	-
48	6084	-	18.40	155.98	-	-	-	-	-	

Table 1. (continued)

No.[a]	ID[b]	Name[c]	Lattitude[d]	Longitude[e]	Radius[f]	R. U.[g]	Nb_O[h]	Nb_S[i]	Nb_S U.[a]	Spatial E.[b]
49	7092	-	24.60	-179.52	-	-	-	-	-	-
50	7092	-	24.94	-179.20	-	60	1	18	10	1.3
51	7092	-	23.90	-179.19	-	-	-	-	-	-
52	-	RS-05	24.15	-179.13	54.5	30	2	16	8	0.56
53	7092	-	24.26	-178.92	-	-	-	-	-	-
54	7092	-	23.38	-178.35	-	-	-	-	-	-
55	7092	-	23.76	-178.29	-	-	-	-	-	-
56	7092	-	24.01	-178.29	59.8	59.8	3	69	25	1.25
57	-	-	23.94	-177.47	-	20	1	5	3	0.38
58	-	-	24.28	-177.39	-	-	-	-	-	-

[a]Number of the deposit, according to Figure 1.
[b]ID and Name of the deposit in *Thomas et al.* [2014a] and/or *Kerber et al.* [2011].
[c]Latitude and longitude of the deposit in degrees, from *Kerber et al.* [2011] and/or *Thomas et al.* [2014a].
[d]Radius of the deposit in kilometers, from *Kerber et al.* [2011] and/or *Thomas et al.* [2014a].
[e]Radius used in the selection of spectra.
[f]Number of MESSENGER/MASCS orbits covering the deposit.
[g]Number of spectra contained in the orbits.
[h]Number of spectra used after removal of outliers spectra.
[i]Maximum allowed extent of the spectra from the vent (the center of the footprint is considered as the value for the spectra). The values are in latitude/longitude from the assumed location of the vent.

The IBD stands for Integrated Band Depth and is comparable in its form to a similar parameter used on the lunar surface to highlight the mineralogical diversity [*Besse et al.*, 2011]. The UV downturn is the parameter introduced by *Goudge et al.* [2014] to characterize the variability of the pyroclastics deposits in the UV range. The VIS and NIR slopes are the slopes of the spectra in each detector. The Color index corresponds to various ratios of wavelengths that have been used in the study of lunar pyroclastics deposits [*Gaddis et al.*, 2003], and also used by *Izenberg et al.* [2014] to characterize the spectral variations of Mercury's surface. The ratios are easy and helpful parameters to distinguish groups of deposits with common characteristics. Finally, the quality index corresponds to the parameters described in section 2.2. Although not designed to be used as parameters to evaluate the properties of the pyroclastics deposits, the quality index can be used to assess the spectral variability within a single deposit.

Table 2. Summary of the Spectral Parameters Used to Highlight the Characteristics of the Pyroclastic Deposits

Name	Spectral Range (nm)	Mathematical Definition
Integrated Band Depth	750–1250	$\sum_{i=750\text{nm}}^{1250_{\text{nm}}} 1-\left(\frac{\text{Reflectance}_{(i)}}{\text{Continuum}_{(i)}}\right)$ Only if $\left(\frac{\text{Reflectance}_{(i)}}{\text{Continuum}_{(i)}}\right)<1$
UV downturn	300–400	$\text{Depth}_{300}+\text{Depth}_{325}+\text{Depth}_{350}$ [*Goudge et al.*, 2014]
VIS slope	445–750	$\left(\frac{750-445}{\text{Reflectance}_{(750)}-\text{Reflectance}_{(445)}}\right)$
NIR slope	1050–1400	$\left(\frac{1400-1050}{\text{Reflectance}_{(1400)}-\text{Reflectance}_{(1050)}}\right)$
Color index	310/390	$\text{Reflectance}_{(310)}/\text{Reflectance}_{(390)}$
	415/750	$\text{Reflectance}_{(415)}/\text{Reflectance}_{(750)}$
	700/1300	$\text{Reflectance}_{(700)}/\text{Reflectance}_{(1300)}$
Quality index	750–800[a]	$\left(\left\langle\sum_{i=750\text{nm}}^{800\text{nm}}\left(\text{Refl}_{\text{Extrapolated}(i)}\right)\right\rangle-\left\langle\sum_{i=750\text{nm}}^{800\text{nm}}\left(\text{Refl}_{(i)}\right)\right\rangle\right)/\left\langle\sum_{i=750\text{nm}}^{800\text{nm}}\left(\text{Refl}_{(i)}\right)\right\rangle*100$
	600–750 and 900–1050[b]	$\left(\frac{750-600}{\text{Refl}_{(750)}-\text{Refl}_{(600)}}\right)/\left(\frac{1050-900}{\text{Refl}_{(1050)}-\text{Refl}_{(900)}}\right)$

[a]Better if value close to zero.
[b]Better if value close to one.

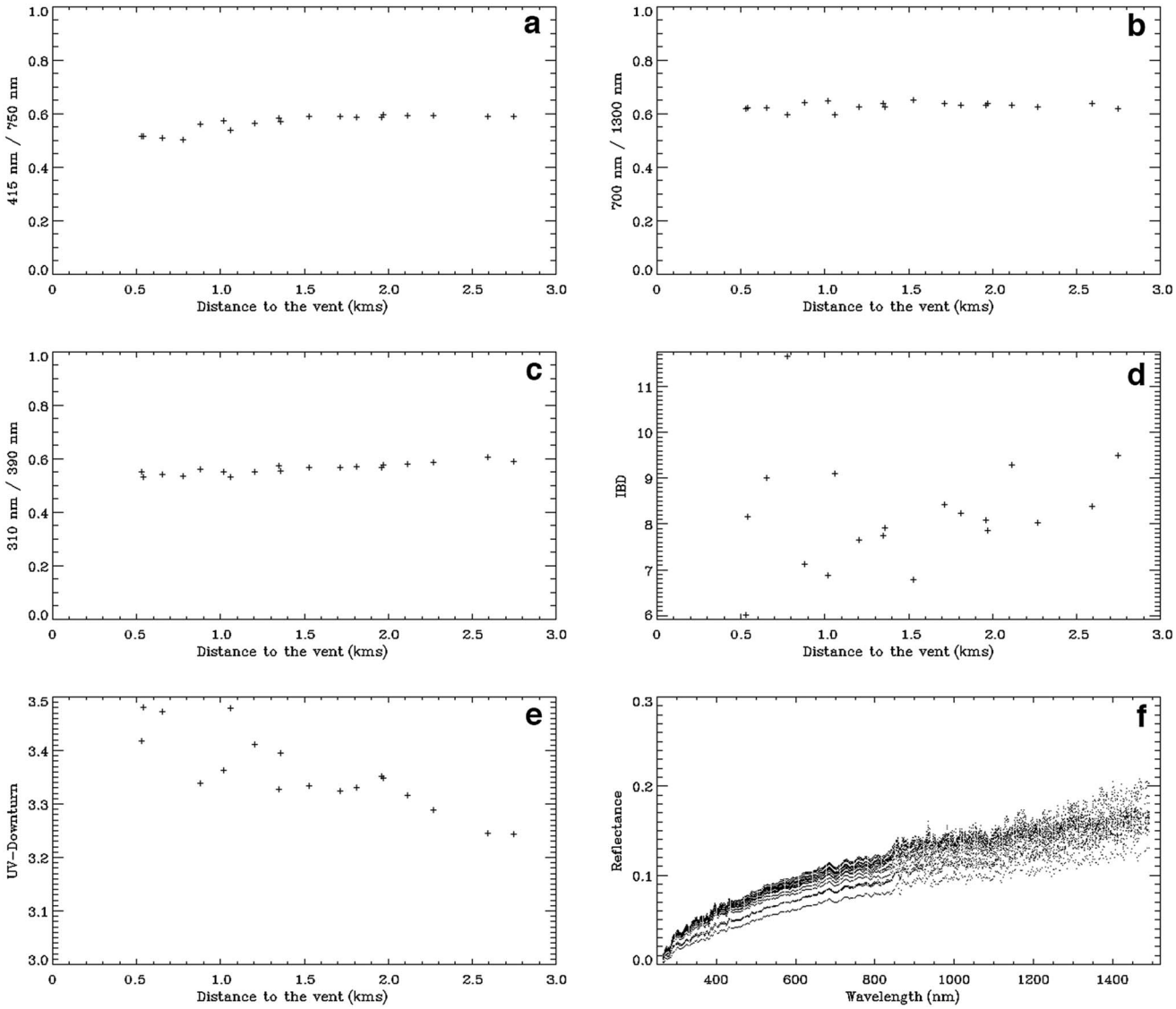

Figure 5. (a–e) Characteristics of spectral parameters as a function of distance from the source, for the point 10 of Figure 1, and the orbit 20121116. Only values for the filtered spectra are plotted (see section 3.1 for detail). The parameters are given in Table 1. (f) Spectra used for this particular orbit.

A few spectra have low-reflectance values that are unlikely to be representative of Mercury's surface, despite exhibiting otherwise normal spectral slopes. The average spectrum of Mercury from *Izenberg et al.* [2014] shows that the reflectance at 575 nm is 0.07 and 0.12 at 1300 nm. To remove the spectra with anomalously low reflectance, two thresholds have been used. Spectra that have a reflectance below 0.01 at 575 nm and below 0.05 at 1300 nm are systematically removed. These values have been defined empirically from the data set used; therefore, some unrepresentative spectra may have not been removed.

Two approaches are used for quality parameters with values defined empirically from the data set used. First, thresholds are defined above which the spectra are not used. For the VIS-NIR slope, quality parameters above 5 and below −1 are considered to be representative of spectra that cannot be adjusted properly by the method defined in section 2.2. Similarly, for the Extrapolation-Real VIS quality factor, a difference greater than 0.5% might be indicative of an inappropriate approach to adjust the spectra, and thus, the spectra are not included. Finally, the remaining spectra that successfully passed the previous criteria should stay within 2 sigma of the mean of the quality parameters within one orbit. This approach is used for both quality parameters and ensures the stability of the spectra used. Ultimately, this process reduces the number of spectra that are used for each deposit, this is reflected in column Nb_S and Nb_S U. of Table 1.

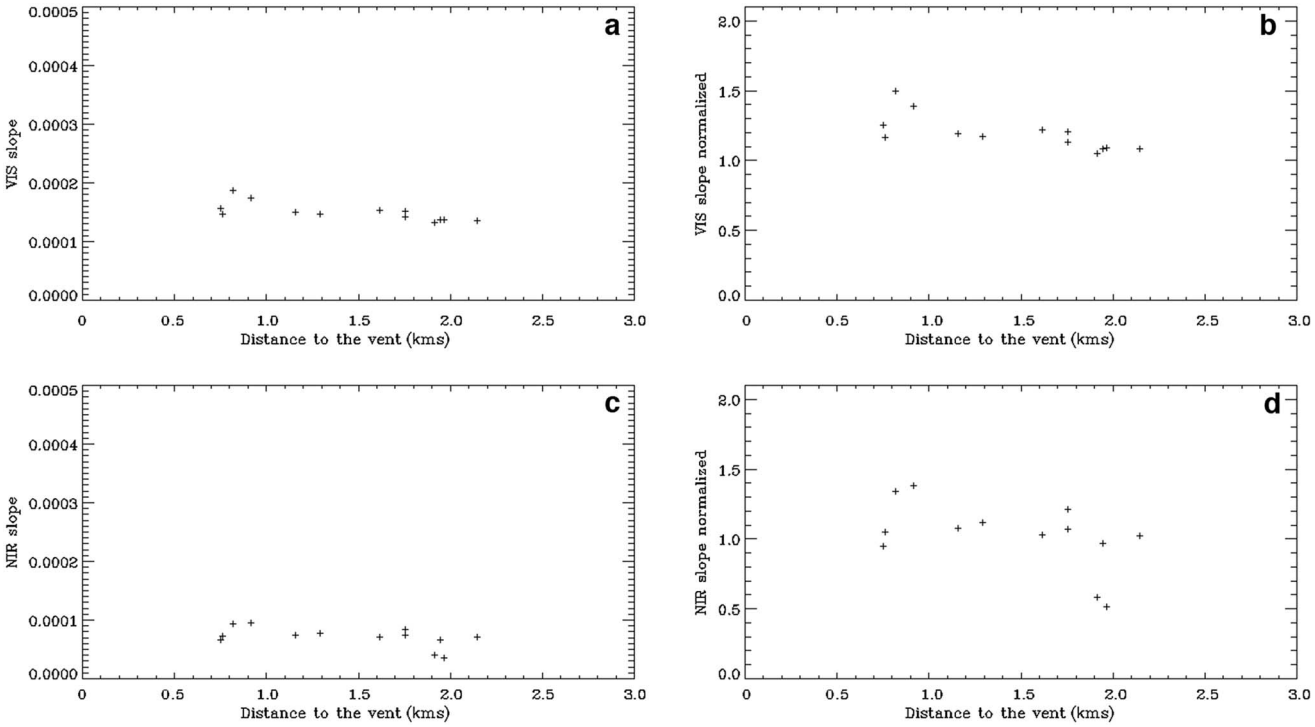

Figure 6. Spectral slopes in the (a, b) VIS and (c, d) NIR domains of the spectra of orbit 20121117 and point 10 of Figure 1. For Figures 6b and 6d, the spectral slopes are normalized by Mercury's average spectrum given in *Izenberg et al.* [2014] to highlight the trend as a function of distance.

3.2. Individual Pyroclastic Deposits

After the spectra are corrected (section 2.2) and filtered (section 3.1), the parameters described in section 3.1 are applied to evaluate the spectral characteristics of each spectrum and pyroclastic deposit candidates. An example for the point 10 of Figure 1, and one specific orbit (i.e., mascs 20121116) is given in Figure 5 as a function of distance from the vent.

Given that a spatial resolution on the order of hundreds of meters can be achieved with MASCS, analysis within the pyroclastic deposits can be done. It is of particular importance to document any variations of the spectral behavior as a function of distance from the volcanic sources. *Jawin et al.* [2015] has shown that in the context of lunar pyroclastic deposits, variations in composition and texture as a function of distance to the vent affect the properties of the spectra. These analyses are important and have not been done in the previous studies of pyroclastic deposits on Mercury [*Kerber et al.*, 2011; *Goudge et al.*, 2014]. In Figure 5, the spectral parameters do not dramatically change as a function of distance to the vent. The distance is defined as the length from the center of the vent to the center of the MASCS footprint (i.e., different spatial resolution could have the same distance to the vent). Nonetheless, the UV downturn parameter displays a correlation with the distance to the vent with value decreasing as footprints are obtained further away from the center of the deposit. This decrease is seen for other pyroclastic deposits within the Caloris basin. The IBD parameter is largely scattered, and no correlations are found with the distance to the vent. This should not be interpreted as a definite answer about the relationship between this parameter and the distance to the source. Given the noise level of the NIR channels, which mostly creates the scatter observed on Figure 5, it is very difficult to identify any absorption. In the analysis of the 31 pyroclastic deposits, the IBD does not show any sign of absorption bands, mostly because of the SNR of the NIR detector.

Previous analyses have highlighted the redder spectral slopes of pyroclastic deposits with respect to the surrounding terrain [*Kerber et al.*, 2011; *Thomas et al.*, 2014b; *Izenberg et al.*, 2014]. Figure 6 highlights this spectral characteristic of the pyroclastic deposits, again using the example of the point 10 with another orbit passing through the same deposit. The spectral slope trend is emphasized when the spectra are normalized by the average spectra of Mercury's surface given in *Izenberg et al.* [2014]. Not only are the pyroclastic deposits redder than the average of Mercury's surface (i.e., >1) but also the decrease in steepness of the slope is strongly correlated to the distance from the vent. This is seen both in the VIS and the NIR domains, although the difference in

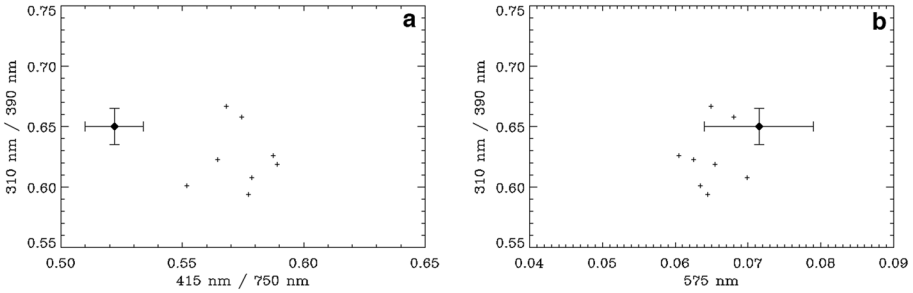

Figure 7. Color properties for the point 27 of Figure 1 and the spectra from all orbits that observed this specific deposit. (a, b) The relative similar characteristics of spectra taken through different location within the pyroclastic deposit. The larger diamond corresponds to Mercury's average spectrum [*Izenberg et al.*, 2014] with the errors bars that highlight Mercury's spectral diversity.

spectral slope in the noisiaer NIR data is less dramatic. As proposed for lunar pyroclastic deposits [*Jawin et al.*, 2015], this correlation with the distance to the vent could be due to the thinning of the pyroclastics deposits, and mixing with the background material.

3.3. Global View on the Caloris Pyroclastic Deposits

Although the spectral properties are correlated to the distance from the source, all the observations of one single pyroclastic deposit candidates could be averaged in an effort to compare the global characteristics of pyroclastic deposits. Although some observations show strong variations within the deposit itself, this variability will be taken into account in the error bars. Similarly to the ratios used by *Izenberg et al.* [2014] and ratios used on the lunar surface with the Clementine observations [*Gaddis et al.*, 2003], color ratios of the deposits are presented in Figure 7 for all orbits covering deposit 47 . The example in Figure 7 is representative of most of the observations, showing that the spectral properties are consistent from orbit to orbit, the difference being mostly due to the intrinsic variability of the deposits (i.e., the footprint close to Mercury's average are located closer to the edges of deposits, thus closer to Mercury's average). Thus, all the spectra of one pyroclastic deposit (from various orbits) are averaged to define its spectral characteristics. The scattering seen in Figure 7 is used to define the error bars.

Figure 8 shows the averaged signal of all pyroclastic deposits individually, with the error bars derived from Figure 7. From the initial number of 58 deposits, 31 have been analyzed. The deposits not analyzed usually do not have coverage with the MASCS instrument. Color ratios have been used by *Izenberg et al.* [2014] to distinguish different types of terrain and could therefore separate the color variability of the pyroclastic deposits, if any exists. From Figure 8, clustering of the pyroclastic deposits is not straight forward, they are strongly correlated with the wavelengths being used. In fact, the UV spectral properties of the pyroclastic deposits are clustered and separated from Mercury's background. This has been already shown in previous studies [*Goudge et al.*, 2014; *Izenberg et al.*, 2014] for different pyroclastic deposits. However, it is important to note that all the deposits analyzed in this study and within the same basin are separated from the average surface, supporting the fact that they should indeed be pyroclastic in origin. Figures 8a, 8b, and 8d highlights clearly the variability of the pyroclastic deposits with respect to Mercury's background within the error bars. Nonetheless, no obvious variability within the pyroclastic deposits in the UV domain could be seen, and deposits from the three different clusters are intimately mixed. The separation of the pyroclastic deposits from Mercury's background is less obvious in the near-infrared domain. The average spectral properties are scattered around Mercury's surface average. This could well be due to the decreased of the SNR in this detector. However, the spread is much more important than the error bars and is therefore most likely highlighting the spectral properties of the pyroclastic deposits. The combination of VIS (700 nm) and VIS/NIR (700/1300 nm) Figure 8e, although not undoubtedly separating the deposits from Mercury's average, is tentatively highlighting trends within the three clusters of deposits. The deposits of the eastern part of the basin (i.e., blue color) show a slight increase in reddening that is correlated with a lower reflectance in the visible with respect to the central cluster (i.e., red color). This trend could also be present when looking specifically in the NIR domain (1400/1200 nm and 1100/1200 nm) Figure 8c. The properties of the western deposits (i.e., black color) exhibit a combination of the properties of the other two clusters, although more of these deposits are closer in characteristics to the central cluster than the eastern cluster.

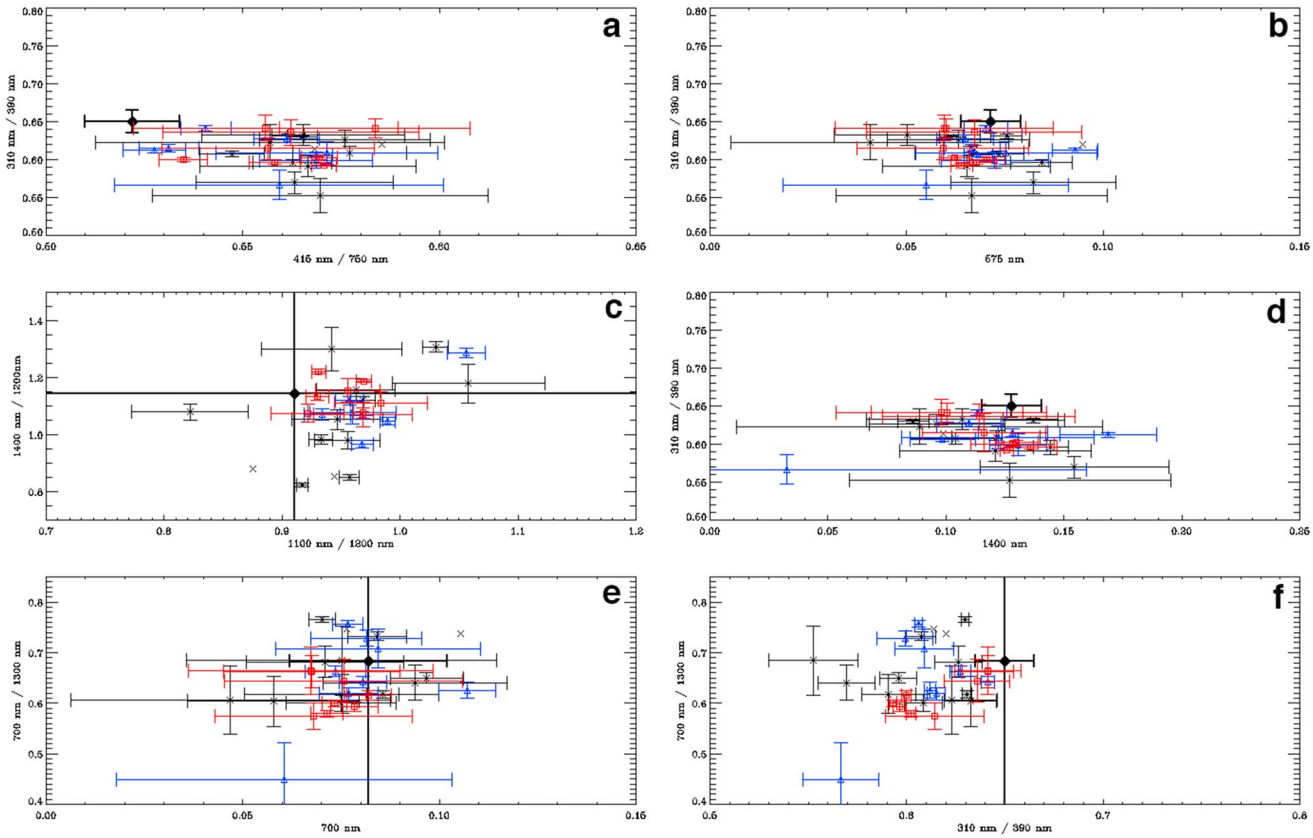

Figure 8. Color properties for the pyroclastic deposits at different wavelengths. (a, b) The trend in the UV(310/390 nm) and the VIS(450/750 nm for Figure 8a, 575 nm for Figure 8b), (c) the trend in the NIR (1400/1200 nm and 1100/1200 nm), (d) compares the UV(310/390 nm) and the NIR (1400 nm), and (e, f) compares the VIS/NIR(700/1300 nm) slopes with the VIS(700 nm, Figure 8e) and the UV(310/390 nm, Figure 8f). Each pyroclastic deposit is an average of all the spectra collected by the MASCS instrument for this point; the error bars correspond to the standard deviation. Black points correspond to the cluster of deposits located on the western side of Caloris (Figure 1), red is for the eastern cluster, and blue is for the central cluster. The larger symbol corresponds to Mercury's average spectrum [*Izenberg et al.*, 2014], with error bars representing Mercury's spectral variability as well as the signal to noise decrease in the NIR.

4. Discussion

Volcanism in the Caloris basin is central to understand the formation of the largest structure on Mercury. *Ernst et al.* [2015] has shown that the thickness of the smooth plains, which are above the low-reflectance material, is very stable throughout the basin. The lack of ghost craters and the fact that most of the massive tectonic modification of the basin occurred after emplacement could imply that the filling of the basin interior by effusive volcanism was relatively quick and widespread in order to sustain this constant thickness. Layering and minerological variability are not seen on the surface of Caloris, and this support the idea of widespread and quick volcanism in Caloris. A counter example is the Imbrium basin on the Moon that has a variety of lava units with different mineralogies and thicknesses [*Thiessen et al.*, 2014], which show unambiguously the volcanic origin of the material filling this basin (the basin itself being created by an impact). The volcanic origin of the pyroclastic deposits of the Caloris basin is more certain, given both the irregular vents and the spectral properties surrounding these vents (Figures 8a, 8b, and 8d). Nonetheless, the question of the compositional variability and age with respect to the age of Mercury's surface and effusive volcanism is key to understand the evolution of the mantle.

When the spatial resolution of the MASCS footprint is small enough, allowing the study of the intrinsic variability of the deposits, it is seen that the value of the UV downturn can change with distance from the vent. The UV downturn values have been interpreted by *Goudge et al.* [2014] as being possibly the effect of oxygen-metal charge transfer [*Burns*, 1993], grain size, and/or space weathering. Given that the UV downturn changes as a function of distance, which could be related to thinning of the deposits [*Jawin et al.*, 2015], it is unlikely that space weathering is the main factor, as already noted by *Goudge et al.* [2014]. It is difficult to explain why a deposit would have differential weathering, although one can argue that the edges of the deposits are mixed

with background material that has undergone various degrees of weathering. Nonetheless, the thinning of the deposits (or increased mixing with the background terrain) could explain both the variation of grain size and/or the composition that will both influence the UV downturn. The increased UV downturn of the pyroclastic deposit with respect to Mercury's average surface suggests that either (1) the iron content of the deposits is lower than Mercury (which is already low in iron) [*Goudge et al.*, 2014; *Kerber et al.*, 2011], given that a decrease in Fe content steepens the UV slopes [*Cloutis et al.*, 2008], or (2) the grain size is dramatically changing with respect to Mercury's background and as a function of distance to the vent as expected for explosive volcanism. Therefore, the decrease of the UV downturn as a function of distance is consistent with both pictures, variability of the composition and/or the grain size. While the deposits are thinning or mixed with the average background of Mercury, the Fe content will slightly increase (in the detection limit of absorption bands in the VIS and NIR wavelengths), which will lower the UV slopes and the UV downturn, as seen in Figure 5. Similarly, decreasing grain size will increase the UV downturn [*Cloutis et al.*, 2008]. Pyroclastic deposits are, as on the Moon [*Wilson and Head*, 1981], probably made of smaller fine grains. Thus, the higher concentration of pyroclastic deposits close to the vent, mostly due to the increased gravity with respect to the Moon [*Kerber et al.*, 2009], will therefore have the same effect of decreasing the UV downturn as a function of distance. Although it is difficult to distinguish between the two possibilities, which are probably both affecting the spectral properties, the decrease of the UV downturn as a function of distance to the vent is consistent with an increase of Fe content and/or an increase in grain size.

Kerber et al. [2011], on the basis of detailed analysis of lunar pyroclastic deposits [*Lucey et al.*, 1995], suggested that the stronger spectral slope of pyroclastic deposits as compared to other volcanic deposits may be an indication of their low iron content. In Figure 8e, a small difference is seen in the average VIS-NIR slope of the deposits, with the eastern deposits being spectrally redder. Following the suggestion of *Kerber et al.* [2011], this could indicate a lower Fe content for this cluster with respect to the central cluster of the Caloris basin. However, the eastern cluster does not show up specifically in the UV ratios, which appear to be a more reliable parameters for Fe content interpretation. Nonetheless, the variability of the spectral slope in the VIS-NIR is still likely separating the eastern and central clusters of deposits, while the western cluster has spectral slopes consistent with both groups. A possible explanation could be in this case the space weathering of the deposits, which could be different depending on the ages of the deposits. With lower spectral slopes, the eastern deposits could potentially be younger than the central cluster. The fact that the western cluster covers both the spectral properties of the central and eastern clusters may show that the age range is in fact much broader for this cluster with both old and young deposits. This age range is consistent with the specific pyroclastic deposit 10 of Figure 1 which is known to have experienced multiple active phases through the same source [*Rothery et al.*, 2014], although no absolute estimation of the time range of activity could be reliably done.

If confirmed, this sequence of varying localized volcanic activity in time and potentially in composition will have implication for the evolution of the interior of Mercury. However, as shown in a recent study [*Knibbe and van Westrenen*, 2015], questions about the internal composition and layering of Mercury's interior are still largely open, thus making more difficult the potential implications of the spectral variability of pyroclastic deposits for Mercury's history.

Although this analysis highlights the intrinsic variability of the pyroclastic deposits within the Caloris basin, high spatial coverage is limited within the extent of the deposit. As such there is insufficient information to analyze in detail the variation of spectral properties as a function of distance. Additionally, the limited excursion in phase angle of the MASCS observations do not help in the identification of the cause of the spectral variability. Nonetheless, the combination of the VIS and NIR wavelengths increases our understanding of the spectral properties of the surface. The next public releases of the MASCS data will increase the number of observations of the pyroclastic deposits to test these results. Ultimately, an analysis of all the deposits on Mercury's surface will also help in understanding the general spectral behavior of these particular volcanic deposits following the proposed improved calibration.

5. Perspectives for the BepiColombo Mission

This detailed analysis of the volcanic deposits of the Caloris basin, with a very large sample of the MASCS observations from the MESSENGER mission, have also highlighted the limitations of such an analysis. The limitations are of different natures and could be significantly improved with the upcoming BepiColombo mission

of the European Space Agency [*Benkhoff et al.*, 2010]. As highlighted in this study, the separation of the VIS and NIR signals in two detectors have created an offset in reflectance that is difficult to correct without assumptions. The Visible and near-Infrared Hyperspectral Imaging channel (VIHI) of the Symbio-Sys instrument suite [*Flamini et al.*, 2010] onboard the BepiColombo mission will cover the range 400 to 2000 nm with one single detector. It is thus expected that the reflectance between the VIS and NIR will be more consistent and facilitate scientific analysis over a large spectral domain. Additionally, the increased domain up to 2000 nm will ensure better coverage of the mafic absorptions with possible hints at the 2000 nm absorption band.

The other difficulties of the MASCS data set are related to the coverage and illumination conditions of the observations. Given that the MASCS instrument is also used to characterize the properties of the exosphere, the coverage of the surface is not continuous. Therefore, there are no orbits covering the surface with nadir observations. Symbio-Sys will be capable of achieving better illumination conditions given its constant nadir pointing to the surface. This will help to improve the spatial coverage and the number of pyroclastic deposits observed during the mission. Additionally, the illumination conditions of the MASCS instrument are not optimal for spectroscopic observations of the surface. With its nadir pointing, observations from the VIHI instrument will be done under illumination conditions more favorable to extract spectroscopic information from the volcanic deposits, and it will also extend the investigations to the southern hemisphere given BepiColombo's different orbit [*Benkhoff et al.*, 2010] with respect to MESSENGER.

It is therefore critical to keep in mind these limitations in the planning of the VIHI observations, in order to maximize the science return of BepiColombo and also increase the number of observations to better interpret the MESSENGER and MASCS observations. Although the lack of iron will still limit the interpretation of the spectra, other instruments onboard the BepiColombo spacecraft will help to provide context and additional information on the mineralogy (e.g., MErcury Radiometer and Thermal infrared Imaging Spectrometer (MERTIS)).

6. Conclusions

The use of the MASCS spectrometer observations of Mercury's surface, although challenging, is very useful in defining the spectral properties of particular features of the surface.

A method is proposed to combine the signal of the UV-VIS and NIR detectors, and specifically to correct the offset of reflectance between the two detectors. This approach relies on the characteristics of the VIS slope, and the assumption that absorption bands are limited on Mercury's surface. Tested on lunar spectra with small absorption bands, the approach has been validated for observations of Mercury's surface. It can extend the observable spectral domain and hence better characterize the spectral properties of the surface. With this proposed correction, spectral characteristics from the UV to NIR can be defined.

Thirty-one Pyroclastic deposits candidates are analyzed within the Caloris basin. They are identified either by spectroscopic anomalies [*Kerber et al.*, 2011] or by the presence of a volcanic vent [*Thomas et al.*, 2014a]. The pyroclastic deposits exhibit several spectroscopic properties that make them distinguishable from the surrounding terrain and Mercury's average surface, thus supporting their volcanic origin:

1. The spectral reddening of the deposits, previously reported [*Kerber et al.*, 2011; *Thomas et al.*, 2014a] based on Mercury Dual Imaging System (MDIS) [*Hawkins et al.*, 2007] images, is also seen with the MASCS observations. Not only are the pyroclastic deposits redder in the VIS domain but they are also redder in the NIR domain. This is consistent with observations of lunar pyroclastic deposits that appear redder than their surroundings in the VIS and NIR [*Besse et al.*, 2014]. However, as seen in Figure 8, the reddening in the NIR could be of different strength, and some pyroclastic deposits match the average spectrum of Mercury in this wavelength domain.
2. Spectral properties of the pyroclastic deposits change as a function of distance to the vent. Both the spectral slope of the VIS and NIR, and the UV downturn decrease when calculated further away from the assumed source. This is consistent with similar characteristics found on lunar pyroclastic deposits [*Jawin et al.*, 2015], and therefore suggests that similar eruption mechanisms (i.e., vulcanian style) could have been the process to produce pyroclastic deposits. Furthermore, this could be an indication of the low iron content of the pyroclastic deposits on Mercury if directly compared to the mineralogical variability of the deposits on the Moon, and/or an indication of the grain size variability with respect to Mercury's background. Space weathering will be more difficult to explain given the intrinsic spectral variability of the deposits.

3. Pyroclastic deposits are easily distinguishable from the surrounding terrain in the UV domain, as previously proposed by *Goudge et al.* [2014]. Spectral properties in the VIS and NIR do not show large variability with the average properties of Mercury's surface.
4. The three main clusters of deposits within the Caloris basin are not easy to distinguish from each other based on their spectroscopic properties. The eastern deposits of the basin have a relatively redder VIS-NIR slope than the deposits from the center or the western part. No distinctions are also seen if a discrimination is made between the identified spectral anomalies [*Thomas et al.*, 2014a; *Kerber et al.*, 2011], and the presence of a volcanic vent [*Thomas et al.*, 2014a]. It is therefore difficult to speculate on the possible timing variability of the pyroclastic deposits within the Caloris basin, although the western deposits probably span over a longer period of time.

Appendix A: Additional Details on the Selection of Spectra and Deposits

Some proposed candidates for pyroclastic deposits are not analyzed, and others are selected with particular conditions.

1. Deposits 1 to 8 do not belong to the three clusters; they are not studied here.
2. Deposit 13 has no orbit in proximity.
3. Deposit 17 has no orbit in proximity.
4. Deposit 20 has the same orbit as 19.
5. Deposit 22 has no orbit in proximity.
6. Deposit 24 has the same orbit as 23.
7. Deposits 30, 32, and 34 have no orbits in proximity.
8. Deposits 36 and 37 have no orbits in proximity.
9. Deposit 39 has no orbit in proximity.
10. Deposit 42 is selected with a larger radius to match MASCS footprint.
11. Deposit 43 is selected as defined by *Thomas et al.* [2014a].
12. Deposits 44 and 45 are selected as defined by *Thomas et al.* [2014a].
13. Deposits 46, 47, and 48 has no orbit in proximity.
14. Deposit 50 is selected (no 49); it is closer to MASCS footprint.
15. Deposit 52 is selected (no 51 and 53); it is defined in *Goudge et al.* [2014].
16. Deposit 56 is selected (no 55 and 54); it is defined in *Thomas et al.* [2014a].
17. Deposit 58 has no orbit in proximity.

Acknowledgments
The ESA fellowship program supported the research of S. Besse. A. Doressoundiram acknowledges the support of CNES. The MASCS data used in this paper are available at the PDS Geosciences Node of Washington University, St. Louis, USA. We are grateful to Rachel Klima, Timothy Glotch, and Carolyn Ernst for helpful comments that improved the quality and clarity of the manuscript. We thank Noam Izenberg for helpful discussion on the calibration of the MASCS instrument. We would like to specifically acknowledge the help of the entire MESSENGER team in providing support for the use of their data set.

References

Benkhoff, J., J. van Casteren, H. Hayakawa, M. Fujimoto, H. Laakso, M. Novara, P. Ferri, H. R. Middleton, and R. Ziethe (2010), BepiColombo—Comprehensive exploration of Mercury: Mission overview and science goals, *Planet. Space Sci.*, *58*, 2–20, doi:10.1016/j.pss.2009.09.020.

Besse, S., J. M. Sunshine, M. I. Staid, N. E. Petro, J. W. Boardman, R. O. Green, J. W. Head, P. J. Isaacson, J. F. Mustard, and C. M. Pieters (2011), Compositional variability of the Marius Hills volcanic complex from the Moon Mineralogy Mapper (M^3), *J. Geophys. Res.*, *116*, E00G13, doi:10.1029/2010JE003725.

Besse, S., et al. (2013), One Moon, many measurements 2: Photometric corrections, *Icarus*, *226*, 127–139, doi:10.1016/j.icarus.2013.05.009.

Besse, S., J. M. Sunshine, and L. R. Gaddis (2014), Volcanic glass signatures in spectroscopic survey of newly proposed lunar pyroclastic deposits, *J. Geophys. Res. Planets*, *119*, 355–372, doi:10.1002/2013JE004537.

Burns, R. G. (1993), Origin of electronic spectra of minerals in the visible to near-infrared region, in *Remote Geochemical Analysis: Elemental and Mineralogical Composition*, edited by C. M. Pieters and P. A. Englert, pp. 3–29, Cambridge Univ. Press, Cambridge, U. K.

Byrne, P. K., C. Klimczak, D. A. Williams, D. M. Hurwitz, S. C. Solomon, J. W. Head, F. Preusker, and J. Oberst (2013), An assemblage of lava flow features on Mercury, *J. Geophys. Res. Planets*, *118*, 1303–1322, doi:10.1002/jgre.20052.

Cloutis, E. A., K. A. McCormack, J. F. Bell, A. R. Hendrix, D. T. Bailey, M. A. Craig, S. A. Mertzman, M. S. Robinson, and M. A. Riner (2008), Ultraviolet spectral reflectance properties of common planetary minerals, *Icarus*, *197*, 321–347, doi:10.1016/j.icarus.2008.04.018.

Denevi, B. W., et al. (2009), The evolution of Mercury's crust: A global perspective from MESSENGER, *Science*, *324*, 613–618, doi:10.1126/science.1172226.

Denevi, B. W., et al. (2013), The distribution and origin of smooth plains on Mercury, *J. Geophys. Res. Planets*, *118*, 891–907, doi:10.1002/jgre.20075.

Ernst, C. M., et al. (2015), Stratigraphy of the Caloris basin, Mercury: Implications for volcanic history and basin impact melt, *Icarus*, *250*, 413–429, doi:10.1016/j.icarus.2014.11.003.

Fassett, C. I., J. W. Head, D. T. Blewett, C. R. Chapman, J. L. Dickson, S. L. Murchie, S. C. Solomon, and T. R. Watters (2009), Caloris impact basin: Exterior geomorphology, stratigraphy, morphometry, radial sculpture, and smooth plains deposits, *Earth Planet. Sci. Lett.*, *285*, 297–308, doi:10.1016/j.epsl.2009.05.022.

Flamini, E., et al. (2010), SIMBIO-SYS: The spectrometer and imagers integrated observatory system for the BepiColombo planetary orbiter, *Planet. Space Sci.*, *58*, 125–143, doi:10.1016/j.pss.2009.06.017.

Gaddis, L. R., M. I. Staid, J. A. Tyburczy, B. R. Hawke, and N. E. Petro (2003), Compositional analyses of lunar pyroclastic deposits, *Icarus*, *161*, 262–280, doi:10.1016/S0019-1035(02)00036-2.

Goudge, T. A., et al. (2014), Global inventory and characterization of pyroclastic deposits on Mercury: New insights into pyroclastic activity from MESSENGER orbital data, *J. Geophys. Res. Planets*, *119*, 635–658, doi:10.1002/2013JE004480.
Hawkins, S. E., et al. (2007), The Mercury dual imaging system on the MESSENGER spacecraft, *Space Sci. Rev.*, *131*, 247–338, doi:10.1007/s11214-007-9266-3.
Head, J. W., et al. (2008), Volcanism on Mercury: Evidence from the first MESSENGER flyby, *Science*, *321*, 69—72, doi:10.1126/science.1159256.
Head, J. W., et al. (2011), Flood volcanism in the northern high latitudes of Mercury revealed by MESSENGER, *Science*, *333*, 1853–1856, doi:10.1126/science.1211997.
Holsclaw, G. M., W. E. McClintock, D. L. Domingue, N. R. Izenberg, D. T. Blewett, and A. L. Sprague (2010), A comparison of the ultraviolet to near-infrared spectral properties of Mercury and the Moon as observed by MESSENGER, *Icarus*, *209*, 179–194, doi:10.1016/j.icarus.2010.05.001.
Izenberg, N. R., et al. (2014), The low-iron, reduced surface of Mercury as seen in spectral reflectance by MESSENGER, *Icarus*, *228*, 364–374, doi:10.1016/j.icarus.2013.10.023.
Jawin, E. R., S. Besse, L. R. Gaddis, J. M. Sunshine, J. W. Head, and S. Mazrouei (2015), Examining spectral variations in localized lunar dark mantle deposits, *J. Geophys. Res. Planets*, *120*, 1310–1331, doi:10.1002/2014JE004759.
Kerber, L., J. W. Head, S. C. Solomon, S. L. Murchie, D. T. Blewett, and L. Wilson (2009), Explosive volcanic eruptions on Mercury: Eruption conditions, magma volatile content, and implications for interior volatile abundances, *Earth Planet. Sci. Lett.*, *285*, 263–271, doi:10.1016/j.epsl.2009.04.037.
Kerber, L., J. W. Head, D. T. Blewett, S. C. Solomon, L. Wilson, S. L. Murchie, M. S. Robinson, B. W. Denevi, and D. L. Domingue (2011), The global distribution of pyroclastic deposits on Mercury: The view from MESSENGER flybys 1–3, *Planet. Space Sci.*, *59*, 1895–1909, doi:10.1016/j.pss.2011.03.020.
Kerber, L., S. Besse, J. W. Head, D. T. Blewett, and T. A. Goudge (2014), The global distribution of pyroclastic deposits on Mercury: The view from orbit, paper presented at 45th Lunar and Planetary Science Conference, 2862 pp., The Woodlands, Tex., 17–21 March.
Klimczak, C., R. A. Schultz, and A. L. Nahm (2010), Evaluation of the origin hypotheses of Pantheon Fossae, central Caloris basin, Mercury, *Icarus*, *209*, 262–270, doi:10.1016/j.icarus.2010.04.014.
Klimczak, C., C. M. Ernst, P. K. Byrne, S. C. Solomon, T. R. Watters, S. L. Murchie, F. Preusker, and J. A. Balcerski (2013), Insights into the subsurface structure of the Caloris basin, Mercury, from assessments of mechanical layering and changes in long-wavelength topography, *J Geophys. Res. Planets*, *118*, 2030–2044, doi:10.1002/jgre.20157.
Knibbe, J. S., and W. van Westrenen (2015), The internal configuration of planet Mercury, paper presented at 46th Lunar and Planetary Science Conference, 1345 pp., The Woodlands, Tex., 16–20 March.
Lucey, P. G., G. J. Taylor, and E. Malaret (1995), Abundance and distribution of iron on the Moon, *Science*, *268*, 1150–1153, doi:10.1126/science.268.5214.1150.
Marchi, S., C. R. Chapman, C. I. Fassett, J. W. Head, W. F. Bottke, and R. G. Strom (2013), Global resurfacing of Mercury 4.0–4.1 billion years ago by heavy bombardment and volcanism, *Nature*, *499*, 59–61, doi:10.1038/nature12280.
McClintock, W. E., and M. R. Lankton (2007), The Mercury atmospheric and surface composition spectrometer for the MESSENGER mission, *Space Sci. Rev.*, *131*, 481–521, doi:10.1007/s11214-007-9264-5.
Murchie, S. L., et al. (2008), Geology of the Caloris basin, Mercury: A view from MESSENGER, *Science*, *321*, 73–76, doi:10.1126/science.1159261.
Murray, B. C., R. G. Strom, N. J. Trask, and D. E. Gault (1975), Surface history of Mercury—Implications for terrestrial planets, *J. Geophys. Res.*, *80*, 2508–2514, doi:10.1029/JB080i017p02508.
Nittler, L. R., et al. (2011), The major-element composition of Mercury's surface from MESSENGER X-ray spectrometry, *Science*, *333*, 1847–1850, doi:10.1126/science.1211567.
Prockter, L. M., et al. (2010), Evidence for young volcanism on Mercury from the third MESSENGER flyby, *Science*, *329*, 668–671, doi:10.1126/science.1188186.
Rothery, D. A., R. J. Thomas, and L. Kerber (2014), Prolonged eruptive history of a compound volcano on Mercury: Volcanic and tectonic implications, *Earth Planet. Sci. Lett.*, *385*, 59–67, doi:10.1016/j.epsl.2013.10.023.
Solomon, S. C., R. L. McNutt, R. E. Gold, and D. L. Domingue (2007), MESSENGER mission overview, *Space Sci. Rev.*, *131*, 3–39, doi:10.1007/s11214-007-9247-6.
Solomon, S. C., R. L. McNutt, and L. M. Prockter (2011), Mercury after the MESSENGER flybys: An introduction to the special issue of Planetary and Space Science, *Planet. Space Sci.*, *59*, 1827–1828, doi:10.1016/j.pss.2011.08.004.
Strom, R. G., et al. (1975), Preliminary imaging results from the second Mercury encounter, *J. Geophys. Res.*, *80*, 2345–2356, doi:10.1029/JB080i017p02345.
Thiessen, F., S. Besse, M. I. Staid, and H. Hiesinger (2014), Mapping lunar mare basalt units in mare Imbrium as observed with the Moon Mineralogy Mapper (M^3), *Planet. Space Sci.*, *104*, 244–252, doi:10.1016/j.pss.2014.10.003.
Thomas, R. J., D. A. Rothery, S. J. Conway, and M. Anand (2014a), Mechanisms of explosive volcanism on Mercury: Implications from its global distribution and morphology, *J. Geophys. Res. Planets*, *119*, 2239–2254, doi:10.1002/2014JE004692.
Thomas, R. J., D. A. Rothery, S. J. Conway, and M. Anand (2014b), Long-lived explosive volcanism on Mercury, *Geophys. Res. Lett.*, *41*, 6084–6092, doi:10.1002/2014GL061224.
Weider, S. Z., L. R. Nittler, R. D. Starr, T. J. McCoy, K. R. Stockstill-Cahill, P. K. Byrne, B. W. Denevi, J. W. Head, and S. C. Solomon (2012), Chemical heterogeneity on Mercury's surface revealed by the MESSENGER X-Ray spectrometer, *J. Geophys. Res.*, *117*, E00L05, doi:10.1029/2012JE004153.
Wilson, L., and J. W. Head (1981), Ascent and eruption of basaltic magma on the Earth and Moon, *J. Geophys. Res.*, *86*, 2971–3001, doi:10.1029/JB086iB04p02971.